Journal of
Nuclear Engineering

MDPI

Article

Time-Dependent Verification of the SP_N Neutron Solver KANECS

Julian Duran-Gonzalez * and Victor Hugo Sanchez-Espinoza

Karlsruhe Institute of Technology (KIT), Institute for Neutron Physics and Reactor Technology (INR), Hermann-von-Helmholtz-Platz 1, 76344 Eggenstein-Leopoldshafen, Germany; victor.sanchez@kit.edu
* Correspondence: julian.gonzalez@kit.edu

Abstract

KANECS is a 3D multigroup neutronics code based on the Simplified Spherical Harmonics (SP_N) approximation and the Continuous Galerkin Finite Element Method (CGFEM). In this work, the code is extended to solve the time-dependent neutron kinetics by implementing a fully implicit backward Euler scheme for the neutron transport equation and an implicit exponential integration for delayed neutron precursors. These schemes ensure unconditional stability and minimize temporal discretization errors, making the method suitable for fast transients. The new formulation transforms each time step into a transient fixed-source problem, which is solved efficiently using the GMRES solver with ILU preconditioning. The kinetics module is validated against established benchmark problems, including TWIGL, the C5G2 MOX benchmark, and both 2D and 3D mini-core rod-ejection transients. KANECS shows close agreement with the reference solutions from well-known neutron transport codes, with consistent accuracy in normalized power evolution, spatial power distributions, and steady-state eigenvalues. The results confirm that KANECS provides a reliable and accurate framework for solving neutron kinetics problems.

Keywords: time-dependent neutron transport; SP_N approximation; finite element method

1. Introduction

Transient analysis in nuclear reactors [1] is essential for safe operation, as it enables evaluation of reactor behavior under accident conditions and provides insight into how the system responds to sudden perturbations. Such transients include reactivity insertions, steam line break, or control rod movements, all of which can lead to rapid changes in the neutron population and power distribution. Therefore, accurate prediction of reactor power evolution determines whether safety limits are exceeded, whether structural damage may occur, and what other consequences may arise. The ability to perform realistic transient simulations is thus an essential part of reactor safety assessment and design verification.

The nuclear transient simulations rely on modeling the time-dependent neutron-kinetics transport equation, which predicts the evolution of the neutron population. To solve this equation, various advanced methods have been developed to approximate its solution. Currently, two approaches [2] are used: Monte Carlo and deterministic methods. Monte Carlo simulations have the advantage of treating very complex three-dimensional geometries without homogenization and of handling the neutron energy spectrum in continuous form. This leads to highly accurate, high-fidelity solutions that can serve as reference calculations. However, such accuracy comes at a high computational cost. Even on massively parallel high-performance computing, fully time-dependent Monte Carlo simulations are

Academic Editor: Eugene Shwageraus

Received: 27 November 2025
Revised: 19 January 2026
Accepted: 27 January 2026
Published: 4 February 2026

limited to very short intervals of real reactor time, often just a few seconds [3]. As a result, they cannot yet be considered practical for the full core transient analysis.

In contrast, deterministic methods provide a more attractive balance between accuracy and computational efficiency. Deterministic solvers are therefore faster and more practical for transient analysis [4] when compared to Monte Carlo methods. Among the available approaches, the Simplified Spherical Harmonics SP_N method [5–7] has emerged as a worthy option. Compared with the traditional diffusion approximation, SP_N achieves superior accuracy in models with strong heterogeneities and high neutron leakage [5], while remaining within a reasonable computational time. This makes it a competitive method for transient applications where both accuracy and performance are critical.

Building on this framework, the Karlsruhe Neutronic Core Simulator (KANECS) [8] has been developed at the Karlsruhe Institute of Technology (KIT) as a multigroup SP_N neutron transport code. KANECS is based on the Continuous Galerkin Finite-Element Method (CGFEM) [9], which provides accurate spatial resolution and robust stability, enabling the modeling of three-dimensional Cartesian reactor geometries. In earlier work, KANECS demonstrated satisfactory results on some steady-state benchmark problems [8], confirming the confidence in its spatial–angular discretization and multigroup treatment for modeling nuclear reactors.

Motivated by these results, the code has recently been extended to include time-dependent capabilities in order to simulate reactor kinetics and transient behavior. In the present work, the transient SP_N equations are integrated using a fully implicit backward Euler time discretization [10]. This widely used approach transforms the original problem into a sequence of transient fixed-source problems, which can then be efficiently solved with a similar steady-state solver. In addition, the delayed neutron precursor equations are integrated using an implicit–exponential scheme to ensure consistent capture of delayed neutron contribution. The overall method yields a first-order, unconditionally stable scheme, making it particularly well-suited for fast transients in which significant changes in reactor conditions occur over timescales.

KANECS is an in-house deterministic neutron transport code developed for nuclear reactor analysis employing high spatial–angular resolution. Although the neutron kinetics equations employed in this work are well established and implemented in several mature neutron core simulator codes, these tools are typically subject to specific access constraints. In this context, the development of KANECS supports the maintenance of independent in-house expertise and methodological know-how, and is intended to complement existing codes by generating additional reference solutions for verification studies. The present work addresses the implementation of a fully implicit transient neutron kinetics capability within this framework through code-to-code comparisons against established reference tools; the objective is not to introduce a new neutron kinetics formulation, but to rigorously verify the time-dependent SP_N implementation in KANECS using well-known benchmark problems.

The paper is organized as follows. Section 2 describes the derivation of the time-dependent SP_N equations and presents the integration within the KANECS framework. Section 3 presents numerical results for a set of widely used benchmark problems to evaluate accuracy and robustness, enabling thorough verification. Finally, a summary, including conclusions and future research perspectives, is provided in Section 4.

2. Methodology

This section presents the numerical treatment of the time-dependent neutron transport equation. First, the Boltzmann and precursor equations are introduced, along with their temporal discretization, where the backward Euler method is used for the neutron flux, and an implicit–exponential approach is employed for the precursors. The equations are

then reformulated using the Simplified Spherical Harmonics (SP_N) approximation and the Continuous Galerkin Finite Element method, resulting in a system of coupled algebraic equations that preserves the structure of the steady-state formulation while enabling transient integration. Finally, the KANECS framework is described, along with the new algorithm developed for transient analysis, including the assembly of the time-dependent operators and the solution strategy.

2.1. Multigroup Time-Dependent Neutron Transport Equation

The transient analysis in this work begins with the multi-group, time-dependent neutron transport equation for the angular flux $\psi_g(\mathbf{r}, \mathbf{\Omega}, t)$ of the energy group g, defined for a multiplicative medium without an external source and under the assumption of isotropic scattering, as written in Equation (1), and it is coupled with the delayed neutron precursor equations of the precursor families N_p, provided by Equation (2).

$$\begin{aligned} &\frac{1}{v_g}\frac{\partial \psi_g(\mathbf{r},\mathbf{\Omega},t)}{\partial t} + \mathbf{\Omega}\cdot\nabla\psi_g(\mathbf{r},\mathbf{\Omega},t) + \Sigma_{t_g}\,\psi_g(\mathbf{r},\mathbf{\Omega},t) \\ &= \sum_{g'=1}^{G} \Sigma_{s_{g'\to g}}\,\phi_{g'}(\mathbf{r},t) + (1-\beta_{tot})\chi_{g_p}\sum_{g'=1}^{G}\nu\Sigma_{f_{g'}}\,\phi_{g'}(\mathbf{r},t) \\ &+ \sum_{i=1}^{N_p}\chi_{g_{d,i}}\,\lambda_i\,C_i(\mathbf{r},t); \quad g = 1,\dots G \end{aligned} \tag{1}$$

$$\frac{\partial C_i(\mathbf{r},t)}{\partial t} = \beta_i \sum_{g'=1}^{G}\nu\Sigma_{f_{g'}}\,\phi_{g'}(\mathbf{r},t) - \lambda_i\,C_i(\mathbf{r},t); \quad i = 1,\dots N_p \tag{2}$$

where

v_g: Neutron speed of group g,
Σ_x: Macroscopic neutron cross-section of type x, t: total; f: fission; s: scattering,
ν: Average number of neutrons emitted per fission,
ϕ_g: Neutron scalar flux,
χ_{g_p}: Prompt fission spectrum of energy group g,
β_{tot}: Delayed neutron total fraction,
$\chi_{g_{d,i}}$: Delayed fission spectrum of energy and precursor groups g, i,
λ_i: Delayed neutron precursor decay constant group i,
C_i: Delayed neutron precursor density group i,
β_i: Delayed neutron fraction group i

For the time discretization of the precursor, Equation (2) is integrated into the interval $[t_k, t_{k+1}]$, where Δt_k is the time step, the implicit–exponential approach is applied, from which it is assumed that the fission source varies slowly over each timestep. Under this assumption, the precursor decay term can be integrated exactly, resulting in the delayed neutron precursor as expressed in Equation (3).

$$C_i^{t_{k+1}}(\mathbf{r}) = e^{-\lambda_i\Delta t_k}C_i^{t_k}(\mathbf{r}) + \frac{\beta_i}{\lambda_i}(1-e^{-\lambda_i\Delta t_k})\sum_{g'=1}^{G}\nu\Sigma_{f_{g'}}^{t_{k+1}}\,\phi_{g'}^{t_{k+1}}(\mathbf{r}); \quad i = 1,\dots N_p \tag{3}$$

Subsequently, the time-dependent neutron transport equation is discretized over the same time interval $[t_k, t_{k+1}]$ using the fully implicit backward Euler method [10], yielding the equation at t_{k+1}. By substituting the precursor concentration from Equation (3) into this discretized neutron transport equation, Equation (4) is obtained, as shown below.

$$\begin{aligned}\boldsymbol{\Omega}\cdot\nabla\psi_g^{t_{k+1}}(\mathbf{r},\boldsymbol{\Omega}) + \left(\frac{1}{v_g\Delta t_k} + \Sigma_{t_g}^{t_{k+1}}\right)\psi_g^{t_{k+1}}(\mathbf{r},\boldsymbol{\Omega}) &= \sum_{g'=1}^{G}\Sigma_{s_{g'\to g}}^{t_{k+1}}\,\phi_{g'}^{t_{k+1}}(\mathbf{r}) \\ + \left[(1-\beta_{tot})\chi_{g_p} + \sum_{i=1}^{N_p}\chi_{g_{d,i}}\,\beta_i\,(1-e^{-\lambda_i\Delta t_k})\right]&\sum_{g'=1}^{G}\nu\Sigma_{f_{g'}}^{t_{k+1}}\,\phi_{g'}^{t_{k+1}}(\mathbf{r}) \\ + \sum_{i=1}^{N_p}\chi_{g_{d,i}}\,\lambda_i\,e^{-\lambda_i\Delta t_k}\,C_i^{t_k}(\mathbf{r}) + \frac{1}{v_g\Delta t_k}\psi_g^{t_k}(\mathbf{r},\boldsymbol{\Omega});&\quad g=1,\dots G\end{aligned} \tag{4}$$

From these equations, it can be observed that if ψ_g^0 and C_i^0 are provided by the initial conditions; then, the solution can be obtained over the entire time domain.

2.2. Time-Dependent Simplified Spherical Harmonics Formulation

The time-dependent SP_N equations preserve the same structure as the formulations introduced in Equations (3) and (4). The procedure for applying the SP_N method, together with the CGFEM, to the time-dependent structure follows a similar approach to that for the steady-state structure, with a detailed derivation described in [8]. Building on this foundation, the extended SP_N time-dependent matrix formulation is presented in Equation (5) (the introduced notations are given in Appendix A). The resulting semidiscrete system yields a set of diffusion-like second-order differential equations, which can be solved using similar methods to those employed for the neutron diffusion equation.

$$\mathbb{V}\frac{\partial}{\partial t}\mathbb{U} - \nabla\cdot\mathbb{D}\nabla\,\mathbb{U} + \mathbb{A}\,\mathbb{U} = \mathbb{F}\,\mathbb{U} + \mathbb{C} \tag{5a}$$

$$\frac{\partial}{\partial t}\mathcal{C}_i = \mathcal{R}_i\Phi_0 - \lambda_i\mathcal{C}_i;\quad i=1,\dots N_p \tag{5b}$$

Here, $\mathbb{U}$ denotes the stacked vector of physical flux moments, $\mathcal{C}_i$ the delayed neutron precursor concentration density of group i, $\mathcal{R}_i$ the precursor production, and Φ_0 the zeroth moment of the neutron flux. With respect to the matrices, $\mathbb{D}$ represents the effective diffusion matrix, $\mathbb{A}$ the absorption matrix, $\mathbb{F}$ the fission production matrix, $\mathbb{V}$ the neutron velocity matrix, and $\mathbb{C}$ the precursor term.

For the spatial discretization, the CGFEM is employed, a well-established method based on a weak formulation of the differential equations that provides numerical stability [11] since the shape functions ensure continuity across element boundaries. In this technique, the neutron flux Φ and the concentration of precursors $\mathcal{C}$ are estimated in Equation (6) as the sum of Lagrange polynomial basis functions $\mathcal{N}$ and multiplied by unknown expansion coefficients $(\widetilde{\Phi}, \mathcal{C}_i)$, where N_{dofs} corresponds to the number of degrees of freedom per element. It is worth noting that increasing the polynomial degree of the shape functions enhances the spatial accuracy of the solution; however, this improvement comes at a higher computational cost due to the large number of degrees of freedom in the elemental matrices.

$$\Phi \approx \sum_{j=1}^{N_{dofs}}\mathcal{N}_j\widetilde{\Phi}_j; \qquad \mathcal{C}_i \approx \sum_{j=1}^{N_{dofs}}\mathcal{N}_j\mathcal{C}_{i,j} \tag{6}$$

As a consequence, matrices from Equation (5) can be constructed into local FEM operator form, as shown in Equation (7), where Ω_c represents the reactor core subdomain, $\partial\Omega_c$ denotes the subdomain surfaces of the reactor boundary, and N_c is the total number of partitioned cells.

$$\widehat{H}_{nn} = \sum_{c=1}^{N_c} \mathbb{D}_{nn} \int_{\Omega_c} \nabla \mathcal{N}_i \cdot \nabla \mathcal{N}_j \, dV - \mathbb{D}_{nn} \int_{\partial\Omega_c} \mathcal{N}_i \nabla \mathcal{N}_j \cdot \hat{n} \, dS + \mathbb{A}_{nn} \int_{\Omega_c} \mathcal{N}_i \mathcal{N}_j \, dV \tag{7a}$$

$$\widehat{H}_{nm} = \sum_{c=1}^{N_c} \mathbb{A}_{nm} \int_{\Omega_c} \mathcal{N}_i \mathcal{N}_j \, dV \quad m \neq n \tag{7b}$$

$$\widehat{F}_{nm} = \sum_{c=1}^{N_c} \mathbb{F}_{nm} \int_{\Omega_c} \mathcal{N}_i \mathcal{N}_j \, dV \tag{7c}$$

$$\widehat{V}_{nm} = \sum_{c=1}^{N_c} \mathbb{V}_{nm} \int_{\Omega_c} \mathcal{N}_i \mathcal{N}_j \, dV \tag{7d}$$

$$\widehat{C}_{n} = \sum_{c=1}^{N_c} \mathbb{C}_{n} \int_{\Omega_c} \mathcal{N}_i \mathcal{N}_j \, dV \tag{7e}$$

Finally, the weak formulation with implicit time discretization yields the following algebraic linear system, as shown in Equation (8). At this point, the equation becomes a transient fixed-source problem at each time step, where the spatial domain boundaries, the Marshak vacuum, and reflective boundary conditions are employed as described in [8]. For the initial state, a steady-state calculation is performed to obtain the initial values of the neutron flux, which, in turn, determine the initial densities of the delayed neutron precursor groups, allowing the transient calculation to be performed in KANECS.

$$\left(\frac{1}{\Delta t_k} \widehat{V}^{t_{k+1}} + \widehat{H}^{t_{k+1}} - \widehat{F}^{t_{k+1}}\right) U^{t_{k+1}} = \widehat{C}^{t_k} + \frac{1}{\Delta t_k} \widehat{V}^{t_k} U^{t_k} \tag{8a}$$

$$\mathcal{C}_i^{t_{k+1}} = \mathcal{C}_i^{t_k} e^{-\lambda i \Delta t_k} + \frac{1 - e^{-\lambda i \Delta t_k}}{\lambda_i} \mathcal{R}_i \Phi_0^{t_{k+1}}; \quad i = 1, \ldots N_p \tag{8b}$$

The time-dependent neutron kinetics equations may be solved using a variety of numerical strategies. In the present work, KANECS employs a multigroup SP_N angular approximation combined with a fully implicit time integration scheme. Compared to explicit or semi-implicit formulations, which may become unstable or require restrictive time-step limitations for stiff transient problems, the fully implicit approach provides unconditional numerical stability and enables robust treatment of reactivity-driven transients. With respect to angular discretization, high-fidelity approaches such as discrete ordinates (S_N) [12] or the method of characteristics (MoC) [2] can achieve high accuracy but are typically associated with substantial computational cost, particularly for time-dependent and high-resolution reactor simulations. The SP_N approximation offers a compromise between transport fidelity and computational efficiency, retaining improved leakage and heterogeneity modeling compared to diffusion theory while avoiding the angular complexity of full transport methods. Consequently, the combination of a fully implicit formulation with the SP_N approximation provides a balanced and robust framework for time-dependent neutron kinetics simulations, suitable for high-resolution forward reactor analysis.

2.3. KANECS Framework

The KANECS code framework [8] is developed using a mix of FORTRAN and C++ languages. KANECS is built on top of three main scientific computing libraries deal.II [13], PETSc [14], and SLEPc [15]. The deal.II finite-element library provides all the frameworks necessary for solving partial differential equations (PDEs), including mesh generation, finite-element coefficients, and degree of freedom management. In the KANECS code, deal.II computes the global indices and the continuous finite-elemental local matrix, which

will be assembled into the global operators. For the resulting global operators, which are typically large and sparse for the SP_N and CGFEM discretizations, the PETSc library plays a key role in solving the algebraic system, as it offers scalable vector and matrix data structures (CRS and matrix-free formats) along with Krylov subspace iterative methods and preconditioner techniques. Finally, for the steady-state criticality calculations, the neutron transport equation is transformed into an eigenvalue problem as Equation (9); hence, the SLEPc library supports eigensolvers, such as the Power Method and the Krylov-Schur method, to obtain solutions for the neutron flux and the effective multiplication factor (k_{eff}).

$$\widehat{H}u = \frac{1}{k_{eff}}\widehat{F}u \tag{9}$$

The time-dependent solution algorithm in KANECS first involves reading the input data (geometry and cross-sections) and then solving the steady-state solution from Equation (9). This step provides the initial flux distribution and the effective multiplication factor; then, in order to make the system critical, the fission term $\nu\Sigma_f$ is divided by k_{eff}. Subsequently, the input kinetic data (delayed neutron fractions (β_i), precursor decay constants (λ_i), and delayed spectra ($\chi_{g_d,i}$)) are read. Later on, the initial delayed neutron precursors source is calculated as Equation (10).

$$\mathcal{C}_i^0 = \frac{\mathcal{R}_i}{\lambda_i}\Phi_0^0; \quad i = 1, \ldots N_p \tag{10}$$

Thereafter, the transient perturbations are applied (cross-sections updated at t_{k+1}), the right-hand side (RHS) at t_k, and the time-dependent transport matrix operator "T" (left-hand side) at t_{k+1} from Equation (8a) are assembled. The resulting linear system is then solved employing the Generalized Minimal Residual (GMRES) method with the Incomplete LU (ILU) preconditioner provided by PETSc. Afterwards, the solution for the t_{k+1} flux is obtained, and a post-processing step is performed, generating a VTK file containing the flux and power distributions at the current time. Finally, the precursors source from Equation (8b) are updated at t_{k+1}, and this procedure is successively repeated until all time steps are swept and is represented in the flowchart in Figure 1.

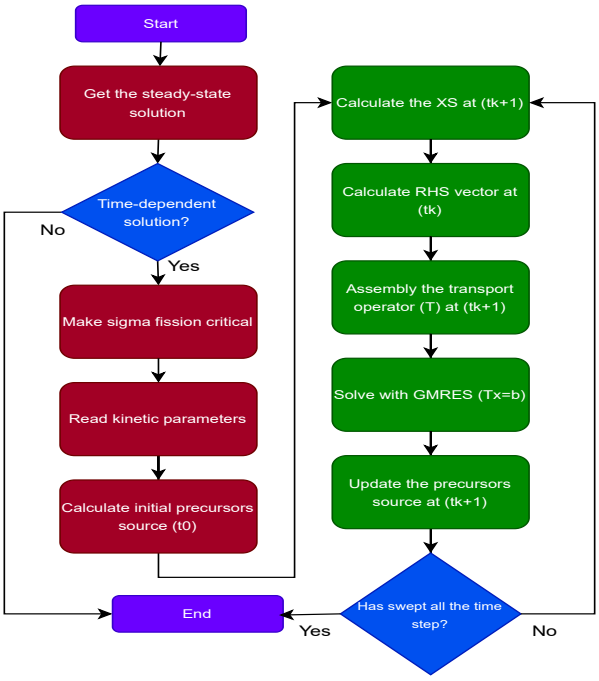

Figure 1. KANECS time-dependent algorithm.

3. Numerical Results

For the KANECS verification, three widely used transient benchmark problems were studied, including the TWIGL benchmark, the C5G2 MOX benchmark, and a homogeneous rodded-assembly ejection transient (mini-core problem). The KANECS simulations are performed using an SP_3 approximation and a finite element polynomial of degree 2. In addition, the results are calculated using convergence tolerances of 10^{-6} for k_{eff} and 10^{-8} for the GMRES method. The time-step size for all transients is fixed at $\Delta t = 10^{-3}$ s. Finally, all calculations were executed on an Intel Core i9-12900 CPU @ 2.40 GHz, 32 GB RAM, running on Ubuntu GNU/Linux 24.04.2 LTS.

3.1. TWIGL Benchmark

The TWIGL benchmark [16] is a two-dimensional reactor composed of three fuel materials with two energy groups based on diffusion theory. The geometry has been simplified with a quarter-core symmetry, and the material distribution and boundary conditions are illustrated in Figure 2. The spatial discretization employs a mesh with 8 cm × 8 cm nodes. The detailed material on neutron cross-sections (originally formulated for diffusion-based codes, the equivalent transport ones were calculated) and neutron delayed data are provided in Tables 1 and 2. The steady-state solution is presented in Table 3, where the result is compared [17] against other well-known deterministic codes, MPACT [18] and DeCART [19], showing excellent agreement with differences of less than 8 pcm.

The transient consists of a material change perturbation in material 1, as described in Table 4. The transient is followed for 0.5 s. The normalized power throughout the transient analysis is shown in Figure 3. As shown, the power follows the behavior expected from the perturbation changes and overlaps with the reference values [17], where the power increases up to its maximum value at 0.2 s and then decreases as a result of the linear material change, reaching its minimum value at 0.4 s. Finalizing, by returning to its initial condition, the power recovers its original value. Additionally, Table 5 presents the region-averaged normalized pin power comparison, in which KANECS agrees well with MPACT and DeCART results, with errors of less than 0.04%. Finally, Figure 4 displays the normalized power distribution in the steady-state, and at the transient, it reaches its maximum value.

Table 1. Neutron cross-section data (cm^{-1}) and velocities (cm/s) for the TWIGL benchmark.

Material	g	Σ_{t_g}	$\Sigma_{s_{g\to g}}$	$\Sigma_{s_{g\to g'}}$	$\nu\Sigma_{f_g}$	v_g
1, 2	1	0.23810	0.21810	0.01000	0.007	1.0×10^7
	2	0.83333	0.00000	0.68333	0.200	1.0×10^5
3	1	0.25641	0.23841	0.01000	0.003	1.0×10^7
	2	0.66667	0.00000	0.61667	0.060	1.0×10^5
4	1	0.23810	0.21810	0.01000	0.007	1.0×10^7
	2	0.81389	0.00000	0.66739	0.200	1.0×10^5
5	1	0.23810	0.21810	0.01000	0.007	1.0×10^7
	2	0.85277	0.00000	0.69927	0.200	1.0×10^5

$\chi_{1_p} = 1.00$, $\chi_{2_p} = 0.00$.

Table 2. Delayed neutron data for the TWIGL benchmark.

i	1
β_i	0.0064
$\lambda_i(s^{-1})$	0.08

$\chi_{1_{d,i}} = 1.00$, $\chi_{2_{d,i}} = 0.00$.

Table 3. Effective multiplication factors for the TWIGL benchmark.

Code	KANECS	MPACT	DeCART
k_{eff}	0.91609	0.91601	0.91605
Δk_{eff}	–	8 pcm	4 pcm

Table 4. Transient perturbation for the TWIGL Benchmark.

Time (s)	Perturbation
$0.0 \rightarrow 0.2$	Linear change: material 1 to 4
$0.2 \rightarrow 0.4$	Linear change: material 4 to 5
$0.4 \rightarrow 0.5$	Step change: material 5 to 1

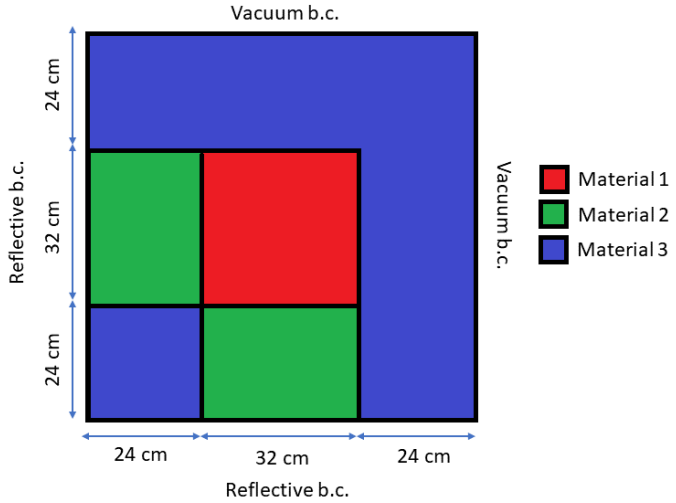

Figure 2. 2D TWIGL reactor configuration.

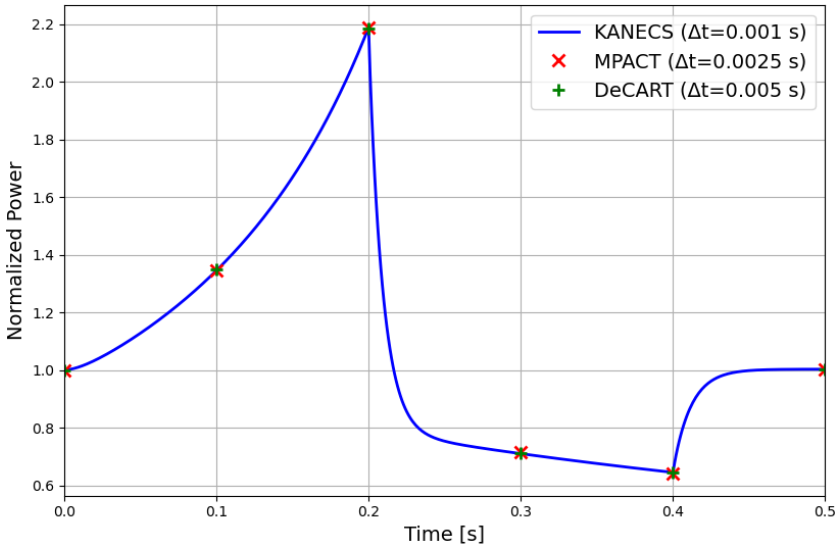

Figure 3. Normalized power results for the TWIGL benchmark.

Table 5. Regional power comparison for the TWIGL benchmark.

Time (s)	Region	KANECS	MPACT	Diff. (%)	DeCART	Diff. (%)
0.0	1	1.5700	1.5699	0.01	1.5698	0.01
	2	1.9937	1.9935	0.01	1.9934	0.02
	3	0.4505	0.4506	−0.02	0.4507	−0.04

Table 5. *Cont.*

Time (s)	Region	KANECS	MPACT	Diff. (%)	DeCART	Diff. (%)
0.1	1	1.5938	1.5937	0.01	1.5936	0.01
	2	1.9818	1.9815	0.02	1.9815	0.02
	3	0.4489	0.4491	−0.04	0.4491	−0.04
0.2	1	1.6184	1.6183	0.01	1.6182	0.01
	2	1.9692	1.9690	0.01	1.9689	0.02
	3	0.4474	0.4475	−0.02	0.4476	−0.04
0.3	1	1.5364	1.5363	0.01	1.5362	0.01
	2	2.0111	2.0109	0.01	2.0108	0.01
	3	0.4525	0.4526	−0.02	0.4527	−0.04
0.4	1	1.5256	1.5255	0.01	1.5255	0.01
	2	2.0167	2.0165	0.01	2.0164	0.01
	3	0.4531	0.4533	−0.04	0.4533	−0.04
0.5	1	1.5700	1.5699	0.01	1.5698	0.01
	2	1.9937	1.9935	0.01	1.9934	0.02
	3	0.4505	0.4506	−0.02	0.4507	−0.04

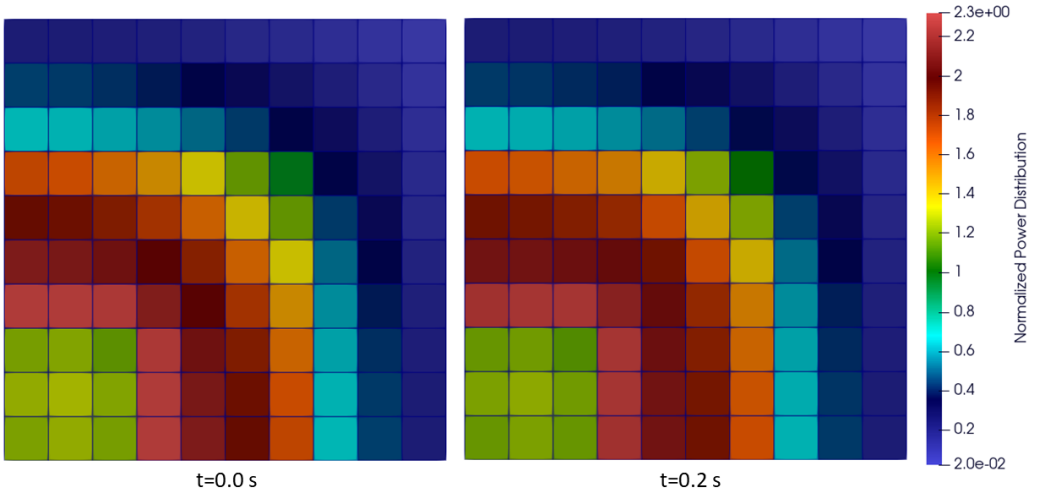

Figure 4. Normalized power distribution for the TWIGL benchmark.

3.2. C5G2 MOX Benchmark

The C5G2 MOX transient benchmark [20] is a two-dimensional configuration based on a variant of the C5G7 [21]. Although it is a simplified version, it provides a more realistic reactor configuration, as it still exhibits a strong spatial gradient due to the UO_2-MOX interfaces, making the diffusion approximation inadequate. The geometry configuration, including material distribution and boundary conditions, is shown in Figure 5. As can be observed, the core configuration consists of 16 square fuel assemblies (UO_2 and MOX types) surrounded by a reflector region, each with a side length of 21.42 cm. Each fuel assembly comprises a 17 × 17 square, homogenized pin cells of side length 1.26 cm. The arrangement of each type of fuel assembly is represented in Figure 6. For the spatial discretization, a pin mesh with a 1.26 cm × 1.26 cm grid is used.

Table 6 contains the two energy group neutron cross-sections for each material. In addition, the detailed specifications of the eight groups of delayed neutrons are given in [21], excluding the delayed neutron spectra, as they were collapsed into two groups; therefore, they are considered equivalent to the prompt spectrum for each precursor. The effective multiplication factor obtained, along with its comparison [22] with the deterministic FEMFFUSION [7] and PARCS [23] codes, is reported in Table 7, with deviations below 10 pcm and 34 pcm, respectively.

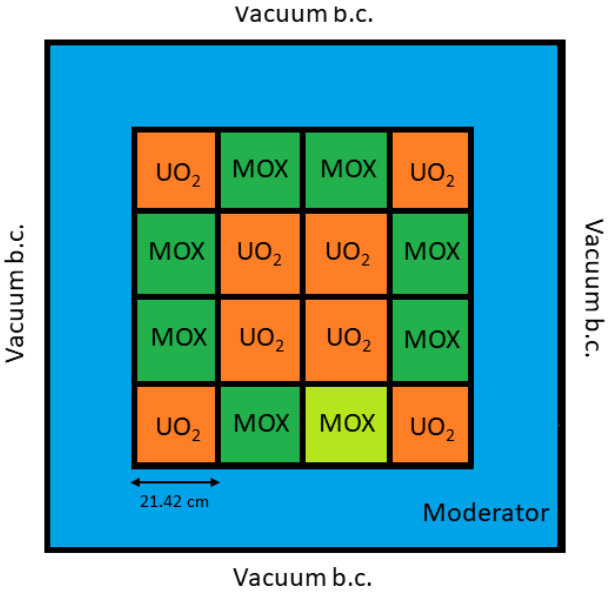

Figure 5. 2D C5G2 MOX core configuration.

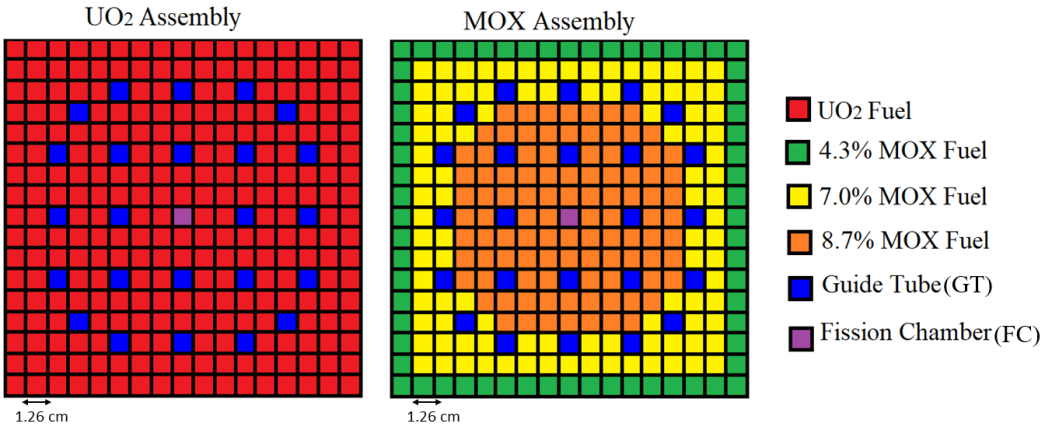

Figure 6. Fuel assemblies configuration for the C5G2 MOX core.

Table 6. Neutron cross-section data (cm^{-1}) and velocities (cm/s) for the C5G2 MOX benchmark.

Material	g	Σ_{t_g}	$\Sigma_{s_{g\to g}}$	$\Sigma_{s_{g\to g'}}$	$\nu\Sigma_{f_g}$	v_g
Moderator	1	0.611	0.560	0.050	0.000	7.73247×10^6
	2	2.340	0.000	2.300	0.000	2.87886×10^5
GT	1	0.586	0.560	0.025	0.000	7.68974×10^5
	2	1.220	0.000	1.200	0.000	2.88616×10^5
FC	1	0.586	0.560	0.025	1.0×10^{-7}	8.73088×10^5
	2	1.220	0.000	1.200	3.0×10^{-6}	2.62899×10^5
UO_2	1	0.570	0.540	0.020	0.0050	7.73247×10^6
	2	1.100	0.000	1.000	0.1250	2.87886×10^5
4.3% MOX	1	0.550	0.520	0.015	0.0075	1.22628×10^7
	2	1.100	0.000	0.900	0.3000	2.88714×10^5
7.0% MOX	1	0.550	0.520	0.015	0.0075	1.46202×10^7
	2	1.010	0.000	0.760	0.3750	2.92249×10^5
8.7% MOX	1	0.550	0.520	0.015	0.0075	1.59499×10^7
	2	1.060	0.000	0.760	0.4500	2.93512×10^5

$\chi_{1_p} = 1.00$, $\chi_{2_p} = 0.00$.

The transient involves a step perturbation, which is defined by replacing the guide tube material in the MOX assembly (marked by a lime-green color; see Figure 5) with a reflector

material, and lasts until 0.05 s. Figure 7 depicts the time evolution of the normalized power. As expected, the power increases because replacing the guide-tube material with a reflector introduces a positive reactivity step, since the reflector has lower absorption. From Table 8, it is observed that the results closely match the FEMFFUSION reference values, with differences below 0.61%, while PARCS-SP_3 shows slightly larger deviations, remaining under 1.20%. Finally, Figure 8 illustrates the normalized power distribution, where the power increase in the perturbed MOX assembly is noticeable.

Table 7. Effective multiplication factors for the C5G2 MOX benchmark.

Code	KANECS	PARCS SP_3	FEMFFUSION
k_{eff}	0.97088	0.97054	0.97078
Δk_{eff}	–	34 pcm	10 pcm

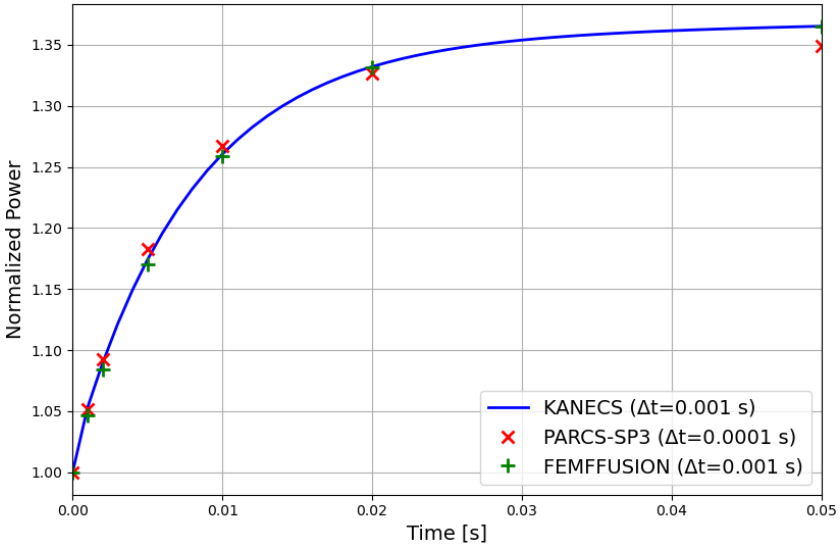

Figure 7. Normalized power results for the C5G2 MOX benchmark.

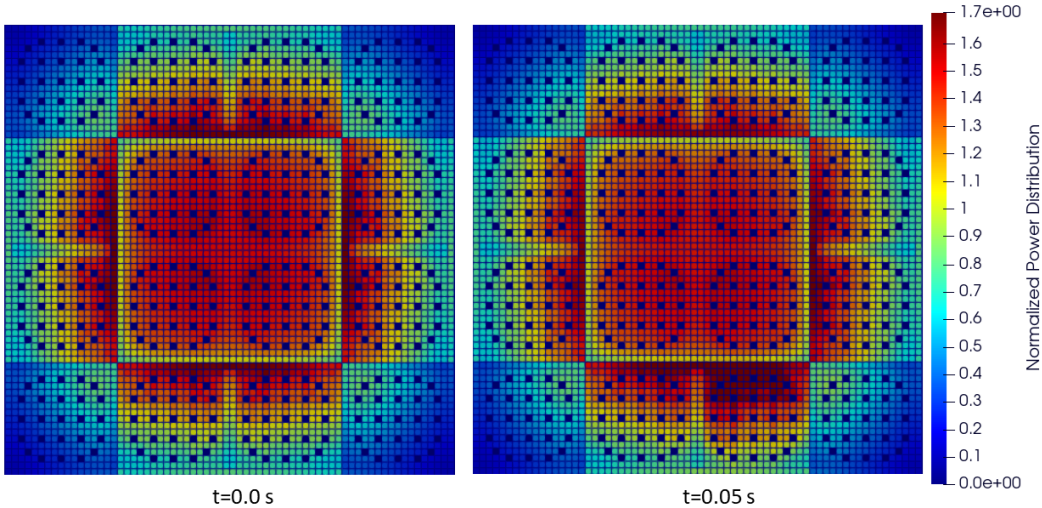

Figure 8. Normalized power distribution for the C5G2 MOX benchmark.

Table 8. Relative power comparison for the C5G2 MOX benchmark.

Time (s)	KANECS	PARCS SP_3	Diff. (%)	FEMFFUSION	Diff. (%)
0.000	1.00000	1.00000	0.00	1.00000	0.00
0.001	1.05312	1.05164	0.14	1.04671	0.61

Table 8. *Cont.*

Time (s)	KANECS	PARCS SP_3	Diff. (%)	FEMFFUSION	Diff. (%)
0.002	1.08937	1.09221	−0.26	1.08409	0.48
0.005	1.17408	1.18305	−0.76	1.17047	0.30
0.010	1.26053	1.26727	−0.53	1.25854	0.15
0.020	1.33214	1.32679	0.40	1.33150	0.04
0.050	1.36524	1.34898	1.20	1.36499	0.01

3.3. Mini-Core Problem

The mini-core problem [19,24] consists of a reactor core composed of a 3 × 3 of homogeneous square assemblies, each with a side length of 21.42 cm. In the 3D configuration, the active core height is 365.76 cm and is enclosed axially by reflectors, each 21.42 cm thick. The geometric configuration and the boundary conditions are illustrated in Figure 9. The two neutron cross-sections and the delayed neutron data are detailed in Tables 9 and 10.

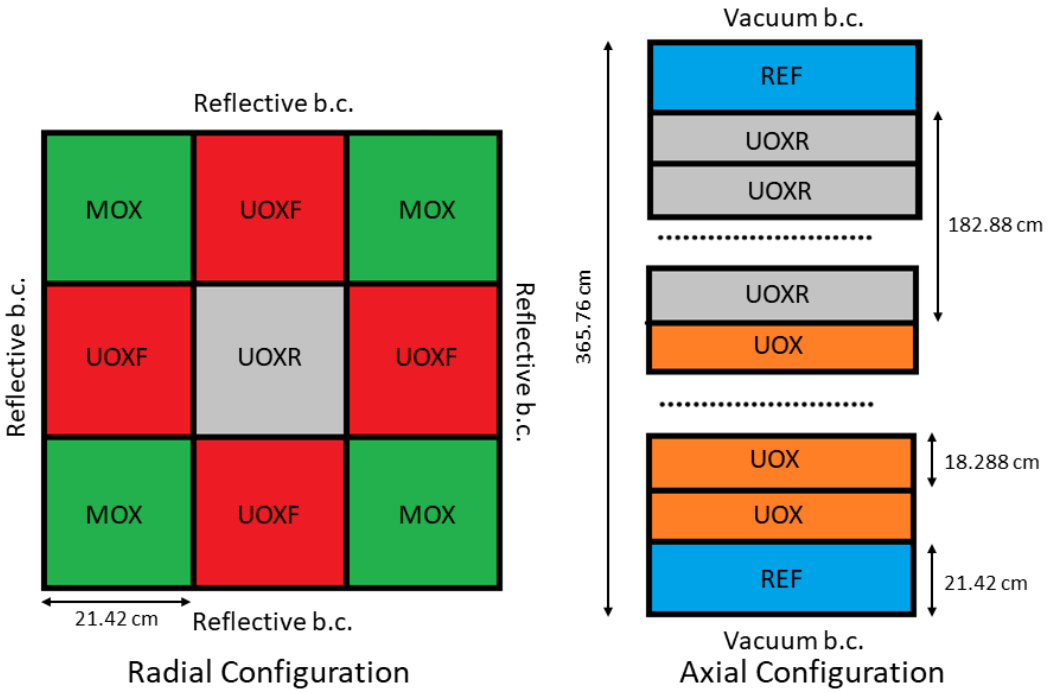

Figure 9. Mini-core problem configuration.

Table 9. Neutron cross-section data (cm^{-1}) and velocities (cm/s) for the mini-core problem.

Material	g	Σ_{t_g}	$\Sigma_{s_{g\to g}}$	$\Sigma_{s_{g\to g'}}$	$\nu\Sigma_{f_g}$	v_g
MOX	1	0.24084	0.21386	0.01485	0.00731	2.8×10^7
	2	0.90380	0.00000	0.69877	0.29250	4.4×10^5
UOXF	1	0.24263	0.21520	0.01749	0.00763	2.8×10^7
	2	0.87901	0.00000	0.76068	0.15789	4.4×10^5
UOX	1	0.23959	0.21197	0.01705	0.00608	2.8×10^7
	2	0.90775	0.00000	0.79258	0.15626	4.4×10^5
UOXR	1	0.23011	0.20051	0.01341	0.00591	2.8×10^7
	2	0.88828	0.00000	0.73738	0.16406	4.4×10^5
UOX-2D	1	0.23011	0.20051	0.01341	0.00591	2.8×10^7
	2	0.88828	0.00000	0.75998	0.16406	4.4×10^5
REF	1	0.30189	0.27194	0.02753	0.00000	2.8×10^7
	2	1.22567	0.00000	1.18843	0.00000	4.4×10^5

$\chi_{1_p} = 1.00$, $\chi_{2_p} = 0.00$.

Table 10. Delayed neutron data for the mini-core problem.

i	1	2	3	4	5	6
β_i	0.00026	0.00152	0.00139	0.00307	0.00110	0.00026
$\lambda_i(s^{-1})$	0.01280	0.03180	0.11900	0.31810	1.40270	3.92860

$\chi_{1_{d,i}} = 1.00$, $\chi_{2_{d,i}} = 0.00$.

3.3.1. Mini-Core 2D Problem

The mini-core 2D problem comprises 4 mixed oxide fresh (UOXF) assemblies, 4 MOX assemblies, and a central control rod (UOXR) assembly. The spatial discretization is performed by dividing each fuel assembly into 6 × 6 nodes. The effective multiplication factor for All Rods Out and All Rods In conditions is listed in Table 11. Compared with other reference codes [19], such as VARIANT [25] and DeCART [19], KANECS results are in excellent agreement with both codes, with differences below 4 pcm for all conditions.

Table 11. Effective multiplication factors for the mini-core 2D problem.

Code	All Rods Out (ARO)			All Rods In (ARI)		
	KANECS	VARIANT	DeCART	KANECS	VARIANT	DeCART
k_{eff}	1.06335	1.06332	1.06331	1.05648	1.05645	1.05644
Δk_{eff}	–	3 pcm	4 pcm	–	3 pcm	4 pcm

The transient perturbation occurs by linearly changing the UOXR material into the UOX-2D material in 0.1 s, and is then followed until 1.0 s. The normalized power results are compared with the references [19], as shown in Figure 10, the results align well with the reference values. Table 12 presents the power comparisons, showing good agreement and finding differences of less than 0.12%. Lastly, Figure 11 shows the power distribution.

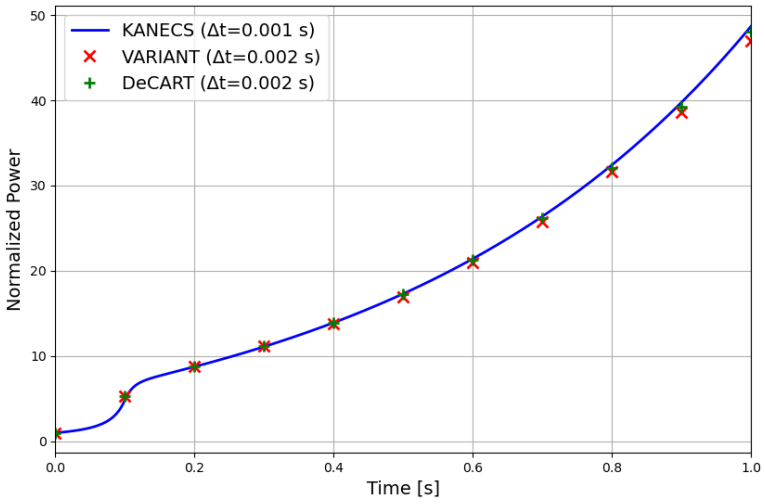

Figure 10. Normalized power results for the mini-core 2D problem.

Table 12. Regional power comparison for the mini-core 2D problem.

Time (s)	Region	KANECS	VARIANT	Diff. (%)	DeCART	Diff. (%)
0.0	UOXR	0.5623	0.5617	0.11	0.5620	0.05
	UOXF	1.0322	1.0334	−0.12	1.0330	−0.08
	MOX	1.0772	1.0761	0.10	1.0760	0.11
1.0	UOXR	0.6603	0.6598	0.08	0.6600	0.05
	UOXF	1.0303	1.0315	−0.12	1.0310	−0.07
	MOX	1.0546	1.0536	0.09	1.0540	0.06

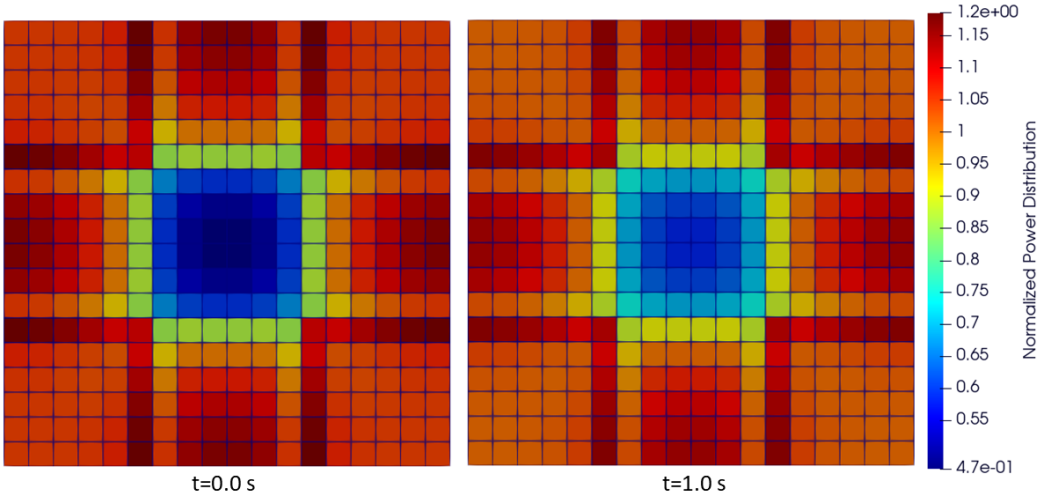

Figure 11. Normalized power distribution for the mini-core 2D problem.

3.3.2. Mini-Core 3D Problem

The mini-core 3D problem features the same spatial mesh radial configuration as the 2D case; however, axially, the UOXR assembly is inserted into half of the assembly size, with the remaining space filled with UOX assembly material (see Figure 9). The axial spatial mesh consists of 20 fuel planes, each 18.288 cm in length, which are internally refined by 2 nodes. The effective multiplication factor comparison is provided in Table 13 for ARO and ARI conditions. The results, once again, are in excellent concordance with the references, with differences of less than 12 pcm.

Table 13. Effective multiplication factors for the mini-core 3D problem.

Code	All Rods Out (ARO)			All Rods In (ARI)		
	KANECS	**VARIANT**	**DeCART**	**KANECS**	**VARIANT**	**DeCART**
k_{eff}	1.08668	1.08664	1.08660	1.08031	1.08026	1.08019
Δk_{eff}	–	4 pcm	8 pcm	–	5 pcm	12 pcm

The transient consists of a rod-ejection event (super-prompt-critical reactivity), in which the control rod is fully withdrawn within 0.1 s. The total transient simulation time is 1.0 s. The resulting normalized power evolution is shown in Figure 12. As observed, the power increases rapidly and continues to increase in the absence of thermal feedback. Furthermore, the rod-cusping effect [26] is negligible in this case because the assemblies are homogeneous. The trend predicted by KANECS closely follows the VARIANT results, but against DeCART, the predictions show a slight deviation while still in good agreement.

The assembly power comparisons are listed in Table 14. As shown, the results closely match the references, with discrepancies below 0.1%. Figure 13 illustrates the power distribution during the rod ejection transient. The power increase is visible throughout the mini-core as the control rod is withdrawn, with initially strong local peaking below the rod position that later spreads more uniformly as the transient progresses. Finally, Figure 14 shows the axial power distribution, which is consistent with the results from VARIANT.

Table 14. Regional power comparison for the mini-core 3D problem.

Time (s)	Region	KANECS	VARIANT	Diff. (%)	DeCART	Diff. (%)
0.0	UOXR	0.9128	0.9125	0.03	0.9120	0.09
	UOXF	1.0270	1.0279	−0.09	1.0280	−0.10
	MOX	0.9948	0.9939	0.09	0.9940	0.08
1.0	UOXR	0.9745	0.9743	0.02	0.9750	0.05
	UOXF	1.0259	1.0267	−0.08	1.0270	−0.11
	MOX	0.9805	0.9797	0.08	0.9800	0.05

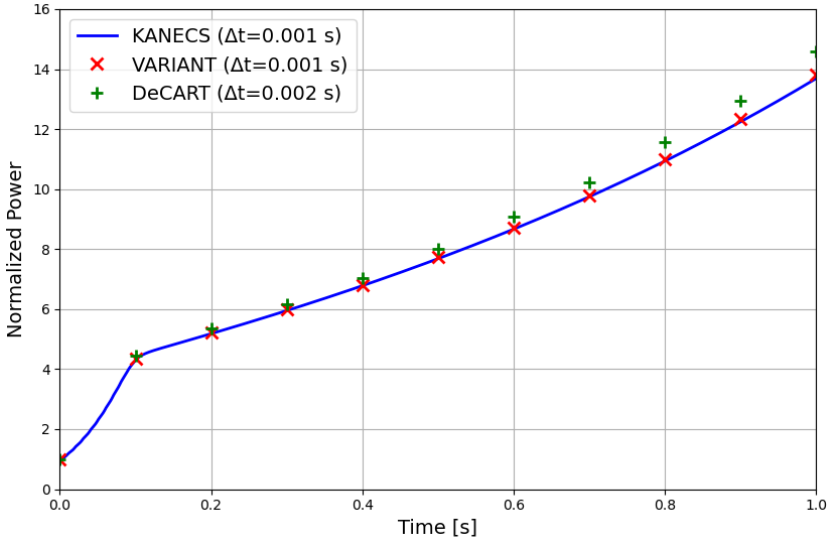

Figure 12. Normalized power results for the mini-core 3D problem.

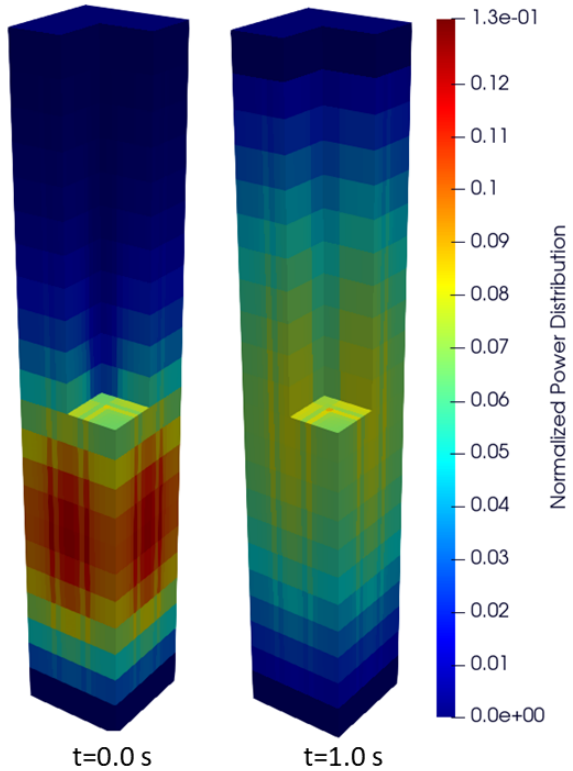

Figure 13. Normalized power distribution for the mini-core 3D problem.

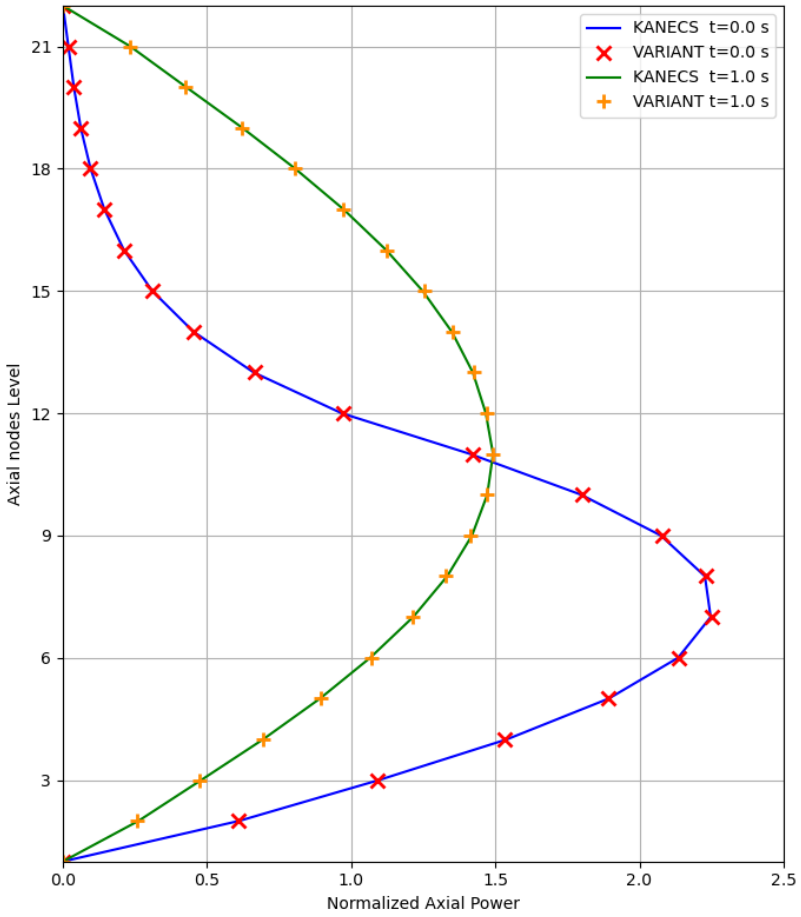

Figure 14. Normalized axial power for the mini-core 3D problem.

4. Conclusions

The time-dependent implementation with explicit representation of delayed neutrons employing the fully backward Euler method was developed into the KANECS neutron code. The kinetics module is validated with well-established benchmarks, such as TWIGL, C5G2 MOX, and Mini-core. Based on numerical solutions from KANECS using the SP_3 approximation and a finite-element polynomial of degree 2, the steady-state and transient predictions demonstrate accurate behavior. Overall, the results show excellent agreement with those from other neutron transport codes, such as MPACT, DeCART, PARCS-SP_3, FEMFFUSION, and VARIANT. The findings demonstrate that KANECS can be considered a promising tool for simulating transient kinetic problems. Future work will include extending a cross-section module in NEMTAB format for coupling with a thermal–hydraulic code for multi-physics simulations, and adding parallelization features to enable full 3D pin-by-pin calculations. In addition, adjoint formulations consistent with time-dependent neutron-kinetics models will be developed to enable sensitivity analysis and support the evaluation of integral kinetics parameters (reactivity, effective delayed-neutron fraction, neutron generation time), as well as subsequent uncertainty quantification and data assimilation studies.

Author Contributions: Conceptualization, J.D.-G. and V.H.S.-E.; methodology, J.D.-G.; software, J.D.-G.; validation, J.D.-G.; formal analysis, J.D.-G.; investigation, J.D.-G.; resources, V.H.S.-E.; data curation, J.D.-G.; writing—original draft preparation, J.D.-G.; writing—review and editing, J.D.-G. and V.H.S.-E.; visualization, J.D.-G.; supervision, V.H.S.-E.; project administration, V.H.S.-E.; funding acquisition, V.H.S.-E. All authors have read and agreed to the published version of the manuscript.

Funding: This research received no external funding.

Data Availability Statement: The original contributions presented in this study are included in the article. Further inquiries can be directed to the corresponding author.

Acknowledgments: The authors acknowledge the financial support of the HGF NUSAFE program at Karlsruhe Institute of Technology (KIT). In addition, we acknowledge support by the KIT Publication Fund of the Karlsruhe Institute of Technology.

Conflicts of Interest: The authors declare no conflicts of interest.

Appendix A

The notations introduced in Equations (5) and (7) are listed below; these correspond to the multi-group SP_7 approximation and were adopted from [6–8].

$$\mathbb{U} = (\, U_1^m, \cdots, U_G^m)^T \tag{A1}$$

$$U^0 = \Phi_0 + 2\Phi_2; \quad U^1 = 3\Phi_2 + 4\Phi_4; \quad U^2 = 5\Phi_4 + 6\Phi_6; \quad U^3 = 7\Phi_6 \tag{A2}$$

$$\mathbb{D} = \mathrm{diag}\,(\, \frac{1}{3\Sigma_1}, \frac{1}{7\Sigma_3}, \frac{1}{11\Sigma_5}, \frac{1}{15\Sigma_7}\,) \tag{A3}$$

$$\Sigma_n = \begin{pmatrix} \Sigma_{t_1} - \Sigma^n_{s_{11}} & -\Sigma^n_{s_{12}} & \cdots & -\Sigma^n_{s_{1G}} \\ \vdots & \vdots & \ddots & \vdots \\ -\Sigma^n_{s_{G1}} & -\Sigma^n_{s_{G2}} & \cdots & \Sigma_{t_G} - \Sigma^n_{s_{GG}} \end{pmatrix} \tag{A4}$$

$$\mathbb{A}_{nm} = \sum_{i=1}^{4} c^{(i)}_{nm}\, \Sigma_i; \quad \mathbb{F}_{nm} = c^{(1)}_{nm}\, F; \quad \mathbb{V}_{nm} = \sum_{i=1}^{4} c^{(i)}_{nm}\, \mathcal{V}; \quad \mathbb{C}_n = d_n \otimes I_G \sum_{i=1}^{Np} \mathcal{M}_i\, \mathcal{C}_i\, e^{-\lambda_i \Delta t_k} \tag{A5}$$

$$c^{(1)} = \begin{pmatrix} 1 & -\frac{2}{3} & \frac{8}{15} & -\frac{16}{35} \\ -\frac{2}{3} & \frac{4}{9} & -\frac{16}{45} & \frac{32}{105} \\ \frac{8}{15} & -\frac{16}{45} & \frac{64}{225} & -\frac{128}{525} \\ -\frac{16}{35} & \frac{32}{105} & -\frac{128}{525} & \frac{256}{1225} \end{pmatrix} \qquad c^{(2)} = \begin{pmatrix} 0 & 0 & 0 & 0 \\ 0 & \frac{5}{9} & -\frac{4}{9} & \frac{8}{21} \\ 0 & -\frac{4}{9} & \frac{16}{45} & -\frac{32}{105} \\ 0 & \frac{8}{21} & -\frac{32}{105} & \frac{64}{245} \end{pmatrix}$$

$$c^{(3)} = \begin{pmatrix} 0 & 0 & 0 & 0 \\ 0 & 0 & 0 & 0 \\ 0 & 0 & \frac{9}{25} & -\frac{54}{175} \\ 0 & 0 & -\frac{54}{175} & \frac{324}{1225} \end{pmatrix} \qquad c^{(4)} = \begin{pmatrix} 0 & 0 & 0 & 0 \\ 0 & 0 & 0 & 0 \\ 0 & 0 & 0 & 0 \\ 0 & 0 & 0 & \frac{13}{49} \end{pmatrix} \tag{A6}$$

$$\nu\Sigma^{crit}_{f_g} = \frac{1}{k_{eff}} \nu\Sigma_{f_g} \tag{A7}$$

$$F = \begin{pmatrix} \chi^{eff}_1 \nu\Sigma^{crit}_{f_1} & \cdots & \chi^{eff}_1 \nu\Sigma^{crit}_{f_G} \\ \vdots & \ddots & \vdots \\ \chi^{eff}_G \nu\Sigma^{crit}_{f_1} & \cdots & \chi^{eff}_G \nu\Sigma^{crit}_{f_G} \end{pmatrix} \tag{A8}$$

$$\chi^{eff}_g = (1 - \beta_{tot})\chi_{g_p} + \sum_{i=1}^{Np} \beta_i (1 - e^{-\lambda_i \Delta t_k}) \chi_{g_{d,i}} \tag{A9}$$

$$\mathcal{V} = \mathrm{diag}\,(\frac{1}{v_1}, \cdots, \frac{1}{v_G}); \qquad d = (\, 1, -\frac{2}{3}, \frac{8}{15}, -\frac{16}{35})^T$$
$$\mathcal{M}_i = (\, \lambda_i\, \chi_{1_{d,i}}, \cdots, \lambda_i\, \chi_{G_{d,i}}\,)^T \qquad \mathcal{R}_i = (\, \beta_i\, \nu\Sigma^{crit}_{f_1}, \cdots, \beta_i\, \nu\Sigma^{crit}_{f_G}\,) \tag{A10}$$

References

1. Cacuci, D.G. (Ed.) *Handbook of Nuclear Engineering*; Springer: New York, NY, USA, 2010. [CrossRef]
2. Azmy, Y.; Sartori, E. *Nuclear Computational Science: A Century in Review*; Springer: Dordrecht, The Netherlands, 2010. [CrossRef]
3. Jaradat, M.K.; Schunert, S.; Gleicher, F.N.; Labouré, V.M.; DeHart, M.D. Forward and inverse predictive transient models of TREAT using surrogate reactivity models. *Ann. Nucl. Energy* **2024**, *201*, 110449. [CrossRef]
4. Böröczki, Z.I.; Klujber, G.; Tolnai, G.; Molnár, B.; Légrády, D.; Gabrielli, F.; Rineiski, A.; Szieberth, M. Simulation of a research reactor reactivity transient with deterministic and GPU-assisted Monte Carlo reactor kinetics codes. *Eur. Phys. J. Plus* **2020**, *135*, 281. [CrossRef]
5. Brantley, P.S.; Larsen, E.W. The Simplified P3 Approximation. *Nucl. Sci. Eng.* **2000**, *134*, 1–21. [CrossRef]
6. Hamilton, S.P.; Evans, T.M. Efficient solution of the simplified PN equations. *J. Comput. Phys.* **2015**, *284*, 155–170. [CrossRef]
7. Fontenla, Y.; Vidal-Ferràndiz, A.; Carreño, A.; Ginestar, D.; Verdú, G. FEMFFUSION and its verification using the C5G7 benchmark. *Ann. Nucl. Energy* **2024**, *196*, 110239. [CrossRef]
8. Duran-Gonzalez, J.; Campos-Muñoz, A.; Sanchez-Espinoza, V.H. Development of the 3D SPN transport solver KANECS for nuclear reactor analysis. *Front. Energy Res.* **2025**, *13*, 1498331. [CrossRef]
9. Zienkiewicz, O.; Taylor, R.; Zhu, J. *The Finite Element Method: Its Basis and Fundamentals*; Butterworth-Heinemann: London, UK, 2005.
10. Stacey, W.M. *Space-Time Nuclear Reactor Kinetics*; Academic Press: New York, NY, USA, 1969; Volume 5. [CrossRef]
11. Hughes, T.J.R. *The Finite Element Method: Linear Static and Dynamic Finite Element Analysis*; Dover Publications: New York, NY, USA, 2000.
12. Duran-Gonzalez, J.; del Valle-Gallegos, E.; Reyes-Fuentes, M.; Gomez-Torres, A.; Xolocostli-Munguia, V. Development, verification, and validation of the parallel transport code AZTRAN. *Prog. Nucl. Energy* **2021**, *137*, 103792. [CrossRef]
13. Arndt, D.; Bangerth, W.; Davydov, D.; Heister, T.; Heltai, L.; Kronbichler, M.; Maier, M.; Pelteret, J.P.; Turcksin, B.; Wells, D. The deal.II finite element library: Design, features, and insights. *Comput. Math. Appl.* **2021**, *81*, 407–422. [CrossRef]
14. Balay, S.; Abhyankar, S.; Adams, M.F.; Benson, S.; Brown, J.; Brune, P.; Buschelman, K.; Constantinescu, E.; Dalcin, L.; Dener, A.; et al. *PETSc/TAO Users Manual*; Technical Report ANL-21/39—Revision 3.23; Argonne National Laboratory: Lemont, IL, USA, 2025. [CrossRef]
15. Hernandez, V.; Roman, J.E.; Vidal, V. SLEPc: A scalable and flexible toolkit for the solution of eigenvalue problems. *ACM Trans. Math. Softw.* **2005**, *31*, 351–362. [CrossRef]
16. Hageman, L.A.; Yasinsky, J.B. Comparison of Alternating-Direction Time-Differencing Methods with Other Implicit Methods for the Solution of the Neutron Group-Diffusion Equations. *Nucl. Sci. Eng.* **1969**, *38*, 8–32. [CrossRef]
17. Zhu, A.; Xu, Y.; Graham, A.; Young, M.; Downar, T.; Cao, L. Transient Methods For Pin-Resolved Whole Core Transport Using The 2D-1D Methodology In MPACT. In *Proceedings of the M&C 2015, Nashville, TN, USA, 19–23 April 2015*; American Nuclear Society: Westmont, IL, USA, 2015.
18. Kochunas, B.; Collins, B.; Jabaay, D.; Downar, T.J.; Martin, W.R. Overview of Development and Design of MPACT: Michigan Parallel Characteristics Transport Code. In *Proceedings of the M&C 2013, London, UK, 3–5 July 2013*; American Nuclear Society: Westmont, IL, USA, 2013.
19. Cho, J.Y.; Kim, K.S.; Lee, C.C.; Zee, S.Q. *Transient Capability of the DeCART Code*; Technical Report KAERI/TR-2930/2005; Korea Atomic Energy Research Institute: Daejeon, Republic of Korea, 2005.
20. Capilla, M.; Talavera, C.; Ginestar, D.; Verdú, G. Validation of the SHNC time-dependent transport code based on the spherical harmonics method for complex nuclear fuel assemblies. *J. Comput. Appl. Math.* **2020**, *375*, 112814. [CrossRef]
21. Hou, J.; Ivanov, K.N.; Boyarinov, V.F.; Fomichenko, P.A. OECD/NEA benchmark for time-dependent neutron transport calculations without spatial homogenization. *Nucl. Eng. Des.* **2017**, *317*, 177–189. [CrossRef]
22. Carreño, A.; Vidal-Ferràndiz, A.; Ginestar, D.; Verdú, G. Time-dependent simplified spherical harmonics formulations for a nuclear reactor system. *Nucl. Eng. Technol.* **2021**, *53*, 3861–3878. [CrossRef]
23. Downar, T.; Xu, Y.; Seker, V. *PARCS v3.0: U.S. NRC Core Neutronics Simulator—Theory Manual*; Technical Report NUREG/CR-7302; U.S. Nuclear Regulatory Commission: Rockville, MD, USA, 2012.
24. Rahman, A. A Comparison Study of the Predictor-Corrector Quasi-static Method and CMFD-based Transient Fixed Source Problem for Transient Analysis. Ph.D. Thesis, Department of Nuclear Engineering, Ulsan National Institute of Science and Technology, Ulsan, Republic of Korea, 2023.
25. Rineiski, A.; Doriath, J.Y. Time Dependent Neutron Transport with Variational Nodal Method. In *Proceedings of the Joint International Conference Mathematical Methods and Supercomputing for Nuclear Applications, Saratoga Springs, NY, USA, 5–9 October 1997*; American Nuclear Society: Westmont, IL, USA, 1997.
26. Joo, H.S. Resolution of the Control Rod Cusping Problem for Nodal Methods. Ph.D. Thesis, Department of Nuclear Engineering, Massachusetts Institute of Technology, Cambridge, MA, USA, 1984.